

OPTIMIZED SCHWARZ METHODS FOR SPHERICAL INTERFACES
WITH APPLICATION TO FLUID-STRUCTURE INTERACTION*GIACOMO GIGANTE[†], GIULIA SAMBATARO[‡], AND CHRISTIAN VERGARA[§]

Abstract. In this work we consider the optimized Schwarz method designed for computational domains that feature spherical or almost spherical interfaces. In the first part, we consider the diffusion-reaction problem. We provide a convergence analysis of the generalized Schwarz method and, following [G. Gigante and C. Vergara, *Numer. Math.*, 131 (2015), pp. 369–404], we discuss an optimization procedure for constant interface parameters leading to a Robin–Robin scheme. Finally, we present some numerical results both in spherical and in ellipsoidal domains. In the second part of the work, we address the fluid-structure interaction problem. Again, we provide a convergence analysis and discuss optimized choices of constant interface parameters. Finally, we present three-dimensional numerical results inspired by hemodynamic applications, to validate the proposed choices in the presence of large added mass effect. In particular, we consider numerical experiments both in an ideal spherical domain and in a realistic abdominal aortic aneurysm.

Key words. optimized Schwarz method, spherical interfaces, fluid structure interaction, abdominal aortic aneurysm

AMS subject classifications. 65N12, 65N30

DOI. 10.1137/19M1272184

1. Introduction. The optimized Schwarz method (OSM) is an effective strategy to solve partial differential equations in a domain decomposition framework [14, 22, 25, 38]. In recent years, several improvements and applications of such a method have been provided by many authors. We mention, for example, the asynchronous update of the interface conditions [28], a posteriori error estimates [2], and GPU-based solutions [27]. Also, analysis and applications for increasingly complex problems have been performed, for example, for the Navier–Stokes equations [5], the gravitational potential problem [27], fluid-structure interaction [17, 20], shallow-water equations [34], Maxwell’s equations [10], and Stokes–Darcy coupling [9].

Another field of study where particular attention has been recently paid is the study of OSM for specific interface morphologies. This has been motivated by concrete applications where usually the interfaces among subproblems are not straight as in standard analyses of OSM. In this respect, we mention [26], where an analysis based on the Steklov–Poincaré operator has been obtained for general interfaces. Moreover, the “half-space, Fourier analysis” has been extended to complex geometries (see [23]), where the method is applied to a Navier–Stokes convection velocity field with circular

*Submitted to the journal’s Methods and Algorithms for Scientific Computing section July 3, 2019; accepted for publication (in revised form) January 31, 2020; published electronically March 17, 2020.

<https://doi.org/10.1137/19M1272184>

Funding: The work of the third author was partially supported by H2020-MSCA-ITN-2017, EU project 765374 “ROMSOC - Reduced Order Modelling, Simulation and Optimization of Coupled systems,” and by the Italian research project MIUR PRIN17 2017AXL54F, “Modeling the heart across the scales: from cardiac cells to the whole organ.”

[†]Dipartimento di Ingegneria Gestionale, dell’Informazione e della Produzione, Università degli Studi di Bergamo, Italy (giacomo.gigante@unibg.it).

[‡]Memphis, Inria Bordeaux Sud-Ouest, France, and Institut de Mathématiques de Bordeaux, Calcul scientifique et Modélisation, France (giulia.sambataro@mail.polimi.it).

[§]LABS, Dipartimento di Chimica, Materiali e Ingegneria Chimica “Giulio Natta,” Politecnico di Milano, Milan, Italy (christian.vergara@polimi.it).

interfaces. See also [16], where it has been shown that for a general interface, one can include the curvature locally in the optimized parameters by using the results from the “straight interface analysis” and a proper scaling (see Remark 3.3 of [16]). The numerical results in [16] show that this approach works well. This would, however, only be an approximation; geometric characteristics of the interface could enter as well into the optimized parameters. In this direction, specific analyses and optimizations have been performed for cylindrical [18, 19, 20, 40] and circular [15, 16, 21] interfaces.

In this work, we consider OSM for a new class of interfaces, namely the spherical ones. This is motivated by the application we have in mind, i.e., hemodynamics, where in some scenarios blood flows in domains which are of almost spherical shape, as happens, for example, in abdominal and cerebral aneurysms and in the heart ventricles [35].

In the first part of the paper, we preliminarily focus on the diffusion-reaction problem (section 2), whereas in the second one we study the fluid-structure interaction (FSI) problem, with the aim of addressing hemodynamic applications (section 3). In both cases, we provide a convergence analysis which allows us to obtain the corresponding reduction factors as a function of the interface symbols characterizing the interface conditions. Several numerical experiments are then shown. In particular, we consider two-dimensional axisymmetric simulations for the diffusion-reaction problem, for both spherical and ellipsoidal domains, and three-dimensional simulations for the FSI case, first in ideal spherical domains and finally in a realistic geometry of an abdominal aortic aneurysm. For all the numerical simulations, optimized interface constant symbols obtained by the abstract optimization procedure developed in [19] are used and compared with other nonoptimized choices.

2. The diffusion-reaction problem.

2.1. Problem setting. Given functions $f \in C^0(\overline{\Omega})$, $\mu \in C^0(\overline{\Omega})$, and $\gamma \in C^0(\overline{\Omega})$,¹ with $\mu > 0$ and $\gamma > 0$, we consider the following problem in the sphere Ω with radius $R + H$: Find u such that

$$(2.1) \quad \begin{aligned} -\mu\Delta u + \gamma u &= f && \text{in } \Omega, \\ u &= 0 && \text{on } \partial\Omega. \end{aligned}$$

Consider now an internal spherical interface Σ (whose center coincides with that of Ω) with radius R and, accordingly, split Ω into two nonoverlapping subdomains, the sphere Ω_1 of radius R and the spherical shell Ω_2 with thickness H .

Then, problem (2.1) can be equivalently written in a multidomain formulation as follows: Find u_1 and u_2 such that

$$(2.2a) \quad -\mu\Delta u_1 + \gamma u_1 = f \quad \text{in } \Omega_1,$$

$$(2.2b) \quad u_1 = u_2 \quad \text{on } \Sigma,$$

$$(2.2c) \quad \mu \frac{\partial u_1}{\partial r} = \mu \frac{\partial u_2}{\partial r} \quad \text{on } \Sigma,$$

¹We provide here the regularity required by the strong formulation of the problem, since the following algorithms are written in this form. However, if one has in mind finite elements for their solution, such hypotheses could be relaxed according to the corresponding weak formulations, e.g., $f \in L^2(\Omega)$, $\mu \in L^\infty(\Omega)$, and $\gamma \in L^\infty(\Omega)$

$$(2.2d) \quad -\mu\Delta u_2 + \gamma u_2 = f \quad \text{in } \Omega_2,$$

$$(2.2e) \quad u_2 = 0 \quad \text{on } \partial\Omega,$$

where r is the radial coordinate.

Introduce now the interface functions S_1 and S_2 . Then, by linearly combining through such functions the interface conditions (2.2b)–(2.2c), we can introduce the following *generalized Schwarz algorithm* for the solution of (2.1): Let $u_2^{(0)}$ be given. Then, at each iteration $k > 0$, until convergence

1. solve the subproblem in Ω_1 ,

$$(2.3a) \quad -\mu\Delta u_1^{(k)} + \gamma u_1^{(k)} = f \quad \text{in } \Omega_1,$$

$$(2.3b) \quad S_1 u_1^{(k)} + \mu \frac{\partial u_1^{(k)}}{\partial r} = S_1 u_2^{(k-1)} + \mu \frac{\partial u_2^{(k-1)}}{\partial r} \quad \text{on } \Sigma;$$

2. then, solve the subproblem in Ω_2 ,

$$(2.4a) \quad -\mu\Delta u_2^{(k)} + \gamma u_2^{(k)} = f \quad \text{in } \Omega_2,$$

$$(2.4b) \quad S_2 u_2^{(k)} + \mu \frac{\partial u_2^{(k)}}{\partial r} = S_2 u_1^{(k)} + \mu \frac{\partial u_1^{(k)}}{\partial r} \quad \text{on } \Sigma,$$

$$(2.4c) \quad u_2^{(k)} = 0 \quad \text{on } \partial\Omega.$$

2.2. Convergence analysis. Referring to Figure 2.1, in view of the convergence analysis of iterations (2.3)–(2.4), we write the Laplacian operator in spherical coordinates as follows:

$$(2.5) \quad \Delta_{sph} = \frac{1}{r^2} \frac{\partial}{\partial r} \left(r^2 \frac{\partial}{\partial r} \right) + \frac{1}{r^2 \sin^2 \varphi} \frac{\partial^2}{\partial \theta^2} + \frac{1}{r^2 \sin \varphi} \frac{\partial}{\partial \varphi} \left(\sin \varphi \frac{\partial}{\partial \varphi} \right).$$

Now, set $\mathbf{x} = r\mathbf{x}'$, where $r = \|\mathbf{x}\|$ and $\mathbf{x}' = \mathbf{x}/\|\mathbf{x}\|$, and let

$$\{P_{m,l}(\mathbf{x}')\}_{m=0,l=1}^{+\infty,k_m}$$

be an orthonormal basis of spherical harmonics of the unit sphere S^2 , where $k_m = (2m+1)$ is the dimension of the eigenspace associated with the eigenvalue $\lambda_m = m(m+1)$, $m = 0, \dots, +\infty$; see, e.g., [13]. Then, for any function $v(\mathbf{x})$, let

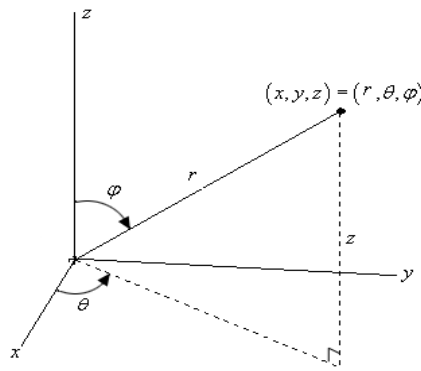


FIG. 2.1. Spherical coordinates.

$$(2.6) \quad \hat{v}(r, m, l) = \int_{S^2} v(r\mathbf{x}') \overline{P_{m,l}(\mathbf{x}')} d\sigma(\mathbf{x}')$$

be its Fourier transform with respect to \mathbf{x}' . Notice that the frequency variable m related to the spatial variable \mathbf{x}' is discrete, since S^2 is a compact manifold.

In view of the convergence analysis, we introduce the modified Bessel functions of first and second kind I_ν and K_ν ; see [24]. Moreover, set

$$(2.7) \quad \alpha = \sqrt{\frac{\gamma}{\mu}}, \quad \chi = \frac{K_{m+\frac{1}{2}}((R+H)\alpha)}{I_{m+\frac{1}{2}}((R+H)\alpha)}.$$

As usual, we set $f = 0$ in order to analyze convergence toward the null solution.

We have the following result.

PROPOSITION 1. *The convergence factor of iterations (2.3)–(2.4) is given by*

$$(2.8) \quad \rho(m) = \left| \frac{\sigma_1(m) - A(m)}{\sigma_2(m) - A(m)} \cdot \frac{\sigma_2(m) - B(m)}{\sigma_1(m) - B(m)} \right|,$$

where

$$(2.9) \quad A(m) = -\mu \frac{2\alpha R K'_{m+\frac{1}{2}}(\alpha R) - K_{m+\frac{1}{2}}(\alpha R) - 2\alpha R \chi I'_{m+\frac{1}{2}}(\alpha R) + \chi I_{m+\frac{1}{2}}(\alpha R)}{2R \left(K_{m+\frac{1}{2}}(\alpha R) - \chi I_{m+\frac{1}{2}}(\alpha R) \right)},$$

$$(2.10) \quad B(m) = -\mu \frac{2\alpha R I'_{m+\frac{1}{2}}(\alpha R) - I_{m+\frac{1}{2}}(\alpha R)}{2R I_{m+\frac{1}{2}}(\alpha R)},$$

and σ_i are the Fourier symbols related to the interface operators S_i , $i = 1, 2$.

Proof. Following [19], by applying the Fourier transform (2.6) to problems (2.3) and (2.4), and by using (2.5), we obtain the following ODEs in the variable r :

$$(2.11) \quad r^2 \frac{\partial^2 \hat{u}_i^{(k)}}{\partial r^2} + 2r \frac{\partial \hat{u}_i^{(k)}}{\partial r} - \left(m(m+1) + \frac{\gamma}{\mu} r^2 \right) \hat{u}_i^{(k)} = 0, \quad i = 1, 2.$$

Through the change of variables $\hat{u}_i^{(k)}(r) = v_i(\alpha r)/\sqrt{r}$, equations (2.11) become

$$v_i''(t) + \frac{1}{t} v_i'(t) - \left(1 + \frac{(m + \frac{1}{2})^2}{t^2} \right) v_i(t) = 0, \quad i = 1, 2.$$

These are modified Bessel equations and their solutions are given by the modified Bessel functions of first and second kind introduced above:

$$v_i(t) = X_{i,1} I_{m+\frac{1}{2}}(t) + X_{i,2} K_{m+\frac{1}{2}}(t), \quad i = 1, 2,$$

for suitable functions of the frequency $X_{i,j}$, $i, j = 1, 2$.

Thus, the Fourier transform of the i th solution at iteration $k > 0$ in the generalized Schwarz algorithm (2.3)–(2.4) assumes the following form:

$$\hat{u}_i^{(k)}(r, m, l) = X_{i,1}^{(k)}(m, l) \frac{I_{m+\frac{1}{2}}(\alpha r)}{\sqrt{r}} + X_{i,2}^{(k)}(m, l) \frac{K_{m+\frac{1}{2}}(\alpha r)}{\sqrt{r}}.$$

Since we assume that the solution u_1 is bounded for $r = 0$, we have

$$(2.12) \quad \widehat{u}_1^{(k)}(r, m, l) = X_1^{(k)}(m, l) \frac{I_{m+\frac{1}{2}}(\alpha r)}{\sqrt{r}}.$$

Instead, due to the homogeneous Dirichlet condition at $\partial\Omega$

$$\widehat{u}_2^{(k)}(R + H, m, l) = X_{2,1}^{(k)}(m, l) \frac{I_{m+\frac{1}{2}}((R + H)\alpha)}{\sqrt{R + H}} + X_{2,2}^{(k)}(m, l) \frac{K_{m+\frac{1}{2}}((R + H)\alpha)}{\sqrt{R + H}} = 0,$$

we have

$$X_{2,1}^{(k)} = - \frac{K_{m+\frac{1}{2}}((R + H)\alpha)}{I_{m+\frac{1}{2}}((R + H)\alpha)} X_{2,2}^{(k)}.$$

Thus, we have

$$(2.13) \quad \widehat{u}_2^{(k)}(r, m, l) = \frac{X_2^{(k)}(m, l)}{\sqrt{r}} \left(K_{m+\frac{1}{2}}(\alpha r) - \chi I_{m+\frac{1}{2}}(\alpha r) \right)$$

with χ given by (3.9).

Inserting the solutions (2.12)–(2.13) into the interface conditions of iterations (2.3)–(2.4) we obtain the following equations:

$$\begin{aligned} & \sigma_1 X_1^{(k)} \frac{I_{m+1/2}(\alpha r)}{r^{1/2}} + \mu X_1^{(k)} \left(\frac{\alpha I'_{m+1/2}(\alpha r)}{r^{1/2}} - \frac{I_{m+1/2}(\alpha r)}{2r^{3/2}} \right) \\ &= \sigma_1 \frac{X_2^{(k-1)}}{r^{1/2}} (K_{m+1/2}(\alpha r) - \chi I_{m+1/2}(\alpha r)) \\ &+ \mu X_2^{(k-1)} \left(\frac{\alpha K'_{m+1/2}(\alpha r) - \chi \alpha I'_{m+1/2}(\alpha r)}{r^{1/2}} - \frac{K_{m+1/2}(\alpha r) - \chi I_{m+1/2}(\alpha r)}{2r^{3/2}} \right), \\ & \sigma_2 \frac{X_2^{(k)}}{r^{1/2}} (K_{m+1/2}(\alpha r) - \chi I_{m+1/2}(\alpha r)) \\ &+ \mu X_2^{(k)} \left(\frac{\alpha K'_{m+1/2}(\alpha r) - \chi \alpha I'_{m+1/2}(\alpha r)}{r^{1/2}} - \frac{K_{m+1/2}(\alpha r) - \chi I_{m+1/2}(\alpha r)}{2r^{3/2}} \right) \\ &= \sigma_2 X_1^{(k)} \frac{I_{m+1/2}(\alpha r)}{r^{1/2}} + \mu X_1^{(k)} \left(\frac{\alpha I'_{m+1/2}(\alpha r)}{r^{1/2}} - \frac{I_{m+1/2}(\alpha r)}{2r^{3/2}} \right). \end{aligned}$$

By computing $X_1^{(k)}$ from the first equation and inserting it into the second one, we can compute the reduction factor defined as $\rho = X_2^{(k)}/X_2^{(k-1)}$ and the thesis follows. \square

2.3. Optimization procedure and choice of the frequencies. In view of the numerical experiments, an optimization procedure is mandatory in order to select reliable values (e.g., among the constants) for the interface parameters σ_1 and σ_2 . Specific optimization procedures could be in principle developed for the problem at hand. These would lead to optimal values of the interface parameters that should make the reduction factor small in comparison to other values for a wide range of frequencies m .

Here, instead, we consider the abstract optimization procedure developed in [19], which provides a range of optimized constant values for the interface parameters, thus leading to an optimized Robin–Robin (RR) scheme. With respect to specific procedures, this one is not able to determine the best choice for the interface parameters, rather only a range of good ones. On the other side, its great advantage is that it is completely general, thus ready to be applied to reduction factors related to a wide class of problems [20, 21].

For the sake of completeness, we review in what follows the abstract optimization procedure reported in [19]. For clarity, we report it directly for the case we have in mind, where only the discrete frequency m is involved.

Assume that the reduction factor has precisely the form of (2.8) with A and B general functions of m . Assume also that $A(m)$ and $B(m)$ are bounded on some set K , with $B < A$ for all $m \in K$, and set

$$(2.14a) \quad \bar{B} = \max_{m \in K} B(m), \quad \bar{A} = \min_{m \in K} A(m),$$

$$(2.14b) \quad \bar{M} = \frac{1}{2}(\bar{A} + \bar{B}), \quad M(m) = \frac{1}{2}(A(m) + B(m)),$$

$$(2.14c) \quad D(m) = \frac{1}{2}(A(m) - B(m)), \quad \bar{Q} = \max_{m \in K} Q(m),$$

$$(2.14d) \quad C = \frac{\min_{m \in K} D(m)}{\max_{m \in K} D(m)}, \quad Q(m) = \frac{|M(m) - \bar{M}|}{D(m)}.$$

The procedure searches optimized values on a specific straight line in the plane σ_1, σ_2 , namely

$$(2.15) \quad \begin{cases} \sigma_1 = p, \\ \sigma_2 = 2\bar{M} - p. \end{cases}$$

In particular, it is proven that, setting

$$\rho_0 = \max \left\{ \left(\frac{1 - \sqrt{C}}{1 + \sqrt{C}} \right)^2; \left(\frac{1 - \sqrt{1 - \bar{Q}^2}}{\bar{Q}} \right)^2 \right\},$$

for all $m \in K$, we have

$$\hat{\rho}(p, m) = \left| \frac{p - A(m)}{-p + 2\bar{M} - A(m)} \frac{-p + 2\bar{M} - B(m)}{p - B(m)} \right| \leq \rho_0 \iff p \in [p_-, p_+]$$

with

$$p_- = \bar{M} + \sup_{m \in K} \left\{ \frac{1 + \rho_0}{1 - \rho_0} D(m) - \sqrt{\left(\bar{M} - M(m) \right)^2 + \frac{4\rho_0}{(1 - \rho_0)^2} (D(m))^2} \right\},$$

$$p_+ = \bar{M} + \inf_{m \in K} \left\{ \frac{1 + \rho_0}{1 - \rho_0} D(m) + \sqrt{\left(\bar{M} - M(m) \right)^2 + \frac{4\rho_0}{(1 - \rho_0)^2} (D(m))^2} \right\}.$$

The strong point of this result is that the range $[p_-, p_+]$ guarantees that the reduction factor is less than ρ_0 for any $m \in K$.

A crucial point from the practical point of view in the application of the previous result is played by the choice of the set of frequencies K . Indeed, different sets lead to different ranges $[p_-, p_+]$. In general, the set K is of the type $[m_{\min}, m_{\max}]$. We discuss in what follows three possible choices of the extreme points of such a range [21].

1. $m_{\min} = 0, m_{\max} = N - 1$. The first choice consists in considering all the admissible frequencies which avoid the aliasing phenomenon for a given computational mesh. In this case $m_{\min} = 0$, whereas we have $m_{\max} = N - 1$, where N is such that simple algebraic considerations ensure that aliasing appears as soon as one replaces $N - 1$ with any bigger number. In particular, by calling Rx_1, \dots, Rx_n the interface mesh nodes and expanding a function with respect to the eigenfunctions of the unit sphere $P_{m,l}$ introduced above, then, for a given function g , the linear system

$$\left\{ \begin{array}{l} g(Rx_1) = \sum_{m=0}^{N-1} \sum_{l=1}^{2m+1} a_{m,l} P_{m,l}(x_1) \\ \dots \\ \dots \\ g(Rx_n) = \sum_{m=0}^{N-1} \sum_{l=1}^{2m+1} a_{m,l} P_{m,l}(x_n) \end{array} \right.$$

does not admit a unique solution if the number of unknowns $a_{m,l}$ (which is $\sum_{m=0}^{N-1} 2m + 1 = N^2$) is greater than the number of equations, i.e., the number of interface points n . Thus, we have that the number of admissible frequencies N is related to the number of interface nodes n by the relation $N = \sqrt{n}$.

2. $m_{\min} = M_{\min}, m_{\max} = M_{\max}$. The second choice is based on observing that among the admissible frequencies $[0, N - 1]$ one expects that only a subset of frequencies $[M_{\min}, M_{\max}]$ could play a major role in determining the reduction factor. This choice could be motivated, for example, by the particular shape of the computational domain or by the problem at hand (pure diffusion, presence of advection, ...). The hope here is that focusing on a smaller effective range of frequencies, the optimization procedure could provide a better range $[p_-, p_+]$ in terms of convergence.
3. $m_{\min} = m_1, m_{\max} = m_2$. The last choice is provided by the minimum and maximum frequencies m_1 and m_2 appearing in the initial guess of the algorithm. The idea is that frequencies outside this range should not give a significant contribution to determining the reduction factor. This could again provide a better range $[p_-, p_+]$.

2.4. Numerical results for the diffusion-reaction problem. We present here some numerical results for the diffusion-reaction problem. These were obtained by considering two-dimensional axisymmetric simulations. In the first test (test I) we consider a spherical computational domain, whereas in the second one (test II) we consider an ellipsoidal domain.

In all the cases, cubic \mathbb{P}_3 Lagrangian finite elements and the open library Freefem++ (www.freefem.org) have been used. Moreover, we set $\mu = \gamma = 1.0$, $f = 0.0$, and the mesh is such that $N = 31$ corresponding to $h = 0.1$. The initial guess is $u_2^{(0)} = \sum_{m=0}^{10} P_m(x/r)$, so that $m_1 = 0$ and $m_2 = 10$. Here, P_m are the Legendre polynomials and $P_m(x/r)$ is the only axisymmetric spherical harmonic corresponding to the frequency variable m . The minimum frequency m_{\min} used in the optimization procedure is always set equal to 0.

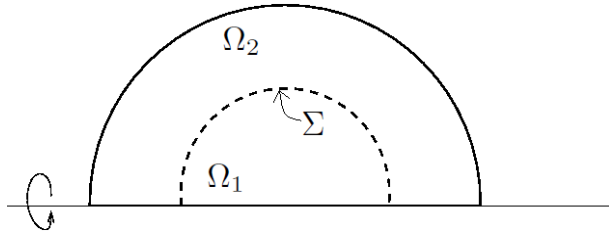


FIG. 2.2. Computational domain for the axisymmetric simulations.

The stopping criterion is given by [3]

$$\int_{\Sigma} \sigma_1 \left| u_1^{(k)} - u_2^{(k)} \right| + \left| \mu \frac{\partial u_1^{(k)}}{\partial r} - \mu \frac{\partial u_2^{(k)}}{\partial r} \right| < \varepsilon$$

with $\varepsilon = 10^{-7}$.

2.4.1. Results in a spherical domain. In this test, Ω is given by the rotation around the x -axis of half of a circle of radius $R_{tot} = 1.5$; see Figure 2.2. The interface Σ is obtained by rotating half of the circumference of radius $R = 1.0$ around the x -axis. Thus, the thickness of the spherical shell Ω_2 is $H = 0.5$.

In what follows we report the convergence properties of numerical simulations obtained for different choices of m_{max} . For each case, the optimized range $[p_-, p_+]$ is evaluated.

1. $m_{max1} = m_2 = 10$. We suppose that the dominant frequencies are those appearing in the initial guess. By applying the optimization procedure, we obtain

$$[p_-, p_+] = [5.669, 5.708], \quad \bar{M} = 1.425, \quad \rho_0 = 0.179.$$

2. $m_{max2} = M_{max} = 20$. We assume that relevant frequencies other than the initial ones appear during the iterations. By applying the optimization procedure, we obtain

$$[p_-, p_+] = [7.386, 7.399], \quad \bar{M} = 1.425, \quad \rho_0 = 0.301.$$

3. $m_{max3} = N - 1 = 30$. We assume that all the admissible frequencies are relevant in determining the reduction factor. By applying the optimization procedure, we obtain

$$[p_-, p_+] = [8.702, 8.710], \quad \bar{M} = 1.425, \quad \rho_0 = 0.378.$$

Notice that in all three cases, the value of \bar{M} is the same, thus the research of the optimized value is obtained by moving along the same straight line $s : \sigma_2 = -\sigma_1 + 2.85$.

In Table 2.1, third column, we report the convergence results for different values of p that are guaranteed to be on this line. In particular, we consider the three optimized values $(\sigma_1^{optj}, 2\bar{M} - \sigma_1^{optj})$, $j = 1, 2, 3$, obtained a priori minimizing, for each of the three estimated ranges, the reduction factor for the values of σ_1 and σ_2 belonging to s , i.e., such that, for $j = 1, 2, 3$,

$$\rho(\sigma_1^{optj}) = \min_{p \in [p_-, p_+]} \max_{m \in [0, m_{maxj}]} \left| \frac{p - A(m)}{-p + 2\bar{M} - A(m)} \frac{-p + 2\bar{M} - B(m)}{p - B(m)} \right|.$$

We also consider other values outside such ranges, still moving along the line s .

TABLE 2.1
Convergence properties for different values of the interface parameters. Test I.

σ_1	$\sigma_2 = 2M - \sigma_1$	# iter	# iter $h/2$	# iter \mathbb{P}_2
$\sigma_1 = 2.00$	$\sigma_2 = 0.85$	54	63	37
$\sigma_1 = 4.00$	$\sigma_2 = -1.15$	17	19	14
$\sigma_1 = \sigma_1^{opt1} = 5.69$	$\sigma_2 = -2.84$	12	14	11
$\sigma_1 = \sigma_1^{opt2} = 7.39$	$\sigma_2 = -4.54$	14	14	14
$\sigma_1 = \sigma_1^{opt3} = 8.71$	$\sigma_2 = -5.86$	17		17
$\sigma_1 = \sigma_1^{opt3} = 11.77$	$\sigma_2 = -8.91$		22	
$\sigma_1 = 10.00$	$\sigma_2 = -7.15$	19	19	19
$\sigma_1 = 12.00$	$\sigma_2 = -9.15$	23	23	22
$\sigma_1 = +\infty$	$\sigma_2 = 0$	92	162	82

From these results we observe that the best optimized value is $p = 5.69$. This value perfectly falls in the first of the three ranges given by the optimization procedure ([5.669, 5.708]), whose extreme points, due to its smallness, in fact provide directly an excellent approximation of the best optimized value. This is consistent with the value of ρ_0 , which is the smallest one among the three estimates. This is probably due to the fact that in this case the smallest frequencies are the most relevant ones, since the initial guess does not contain frequencies greater than 10. Thus, in the optimization procedure it is enough to consider as maximum frequency m_{max} , i.e., the greatest one appearing in the initial condition.

We notice also the great improvement of the generalized Schwarz (Robin–Robin) algorithm with respect to the Dirichlet–Neumann (DN) one ($\sigma_1 = +\infty$, $\sigma_2 = 0$) with an Aitken acceleration procedure [7, 36].

To check the qualitative robustness of these results with respect to the space discretization, we run the same cases for a value of the mesh size which is half of the previous one, that is, for $h = 0.05$ corresponding to $N = 62$. Notice that in this case only the values of σ_j^{opt3} change due to the change of the mesh size. The results are reported in the fourth column of Table 2.1. We also run the numerical experiments for \mathbb{P}_2 Lagrangian finite elements with the reference value of the mesh size. The results are reported in the last column of Table 2.1. We notice in any case a good accordance with respect to the behavior highlighted by the reference case.

To go deeper into the analysis of the results, we report in Figure 2.3, left, the quantity $\hat{\rho} = \max_{m \in [0, 10]} \rho(m)$, with ρ given by (2.8)–(2.9)–(2.10), as a function of σ_1 and σ_2 . The values of $\hat{\rho}$ are obtained with an a priori (no computational) analysis performed in Scilab. From this figure, we have a clear picture of the behavior of the reduction factor $\hat{\rho}$, which features two minima (contour lines in black). In particular, we notice a certain symmetry of the contour lines with respect to the straight line chosen to search the optimized value and given by (2.15). This justifies our choice which misses the two minima but, looking for a balanced approximation, it is able to find a very good result (see red circle).

The same behavior is found in Figure 2.3, right, where the number of iterations obtained by numerical experiments is reported as a function of σ_1 and σ_2 .

2.4.2. Results in an ellipsoidal domain. In the next numerical experiment, we consider a computational domain which is not a sphere. Indeed, our hope is that our spherical analysis and optimization procedure provide effective values of the interface parameters also for nonspherical interfaces, provided that the shape of the domain

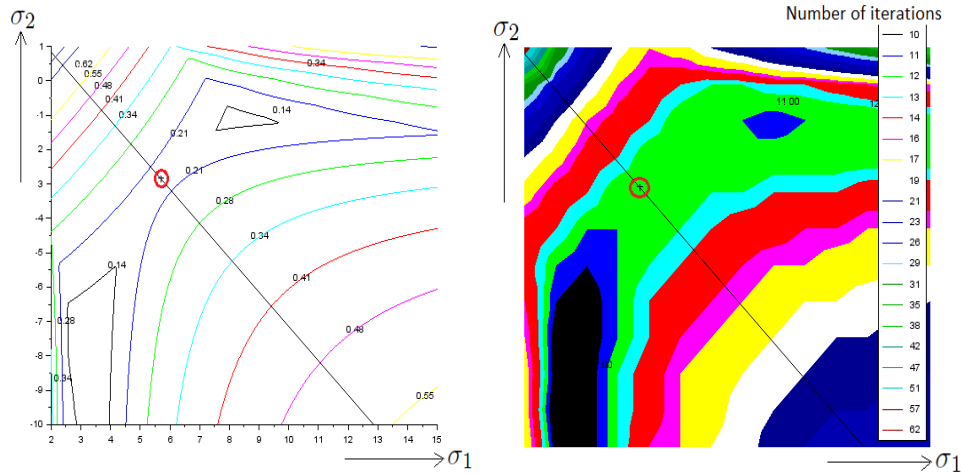


FIG. 2.3. Left: Contour lines of values of $\hat{\rho}$ for $m \in [0, 10]$ as a function of σ_1 and σ_2 . Right: Number of iterations as a function of σ_1 and σ_2 . In both cases, the straight line given by (2.15) and the optimized value $(\sigma_1^{\text{opt1}}, \sigma_2^{\text{opt1}})$ (in the red circle) are reported.

TABLE 2.2
Number of iterations for the ellipsoidal domain. Left: $a = 1.5, b = 1.2$. Right: $a = 3.0, b = 1.2$.
 Test II.

	ρ_0	σ_1^{opt}	σ_2^{opt}	# iter	ρ_0	σ_1^{opt}	σ_2^{opt}	# iter
$R = a$	0.12	4.57	-2.18	11	0.04	3.30	-1.47	9
$R = b$	0.15	5.14	-2.51	12	0.15	5.14	-2.51	13
$R = \frac{a+b}{2}$	0.13	4.83	-2.32	11	0.08	3.87	-1.78	10
$R = \sqrt{ab}$	0.14	4.84	-2.33	11	0.09	4.06	-1.89	11

and of the interface is almost spherical. In this case, we do not obtain the optimized values for such a configuration, but we expect to obtain excellent approximations.

To this aim, we consider an ellipsoidal domain with semiaxis equal to $a + H$, $b + H$, and $b + H$ for the x , y , and z directions, respectively, obtained by a rotation around the x -axis of the ellipse with semiaxis equal to $a + H$ (x -direction) and $b + H$ (y -direction). The interface Σ is obtained by rotating around the x -axis half of the ellipse with semiaxis of length a and b .

For the choice of the radius of the sphere to be used in the analysis and optimization procedure for the computation of A and B in (2.9)–(2.10), we study the numerical performance of four different choices: $R = a$, $R = b$, $R = (a + b)/2$, $R = \sqrt{ab}$, i.e., the two values of the semiaxes and the two means, the arithmetic and the geometric ones. We set $m_{max} = m_2 = 10$.

In Table 2.2 we report the convergence properties of two numerical tests, one for an ellipsoidal domain with a very low eccentricity ($a = 1.5, b = 1.2$), and the other one with a greater value of the eccentricity ($a = 3.0, b = 1.2$). The optimized values of σ_1 and σ_2 and the corresponding reduction factor have been found within the range of values belonging to a straight line, as described above. From these results, we observe that when the eccentricity is low, all the choices proposed to estimate R in the optimization procedure work well. For an increased eccentricity, we observe instead some differences among the four choices, in particular $R = a$, i.e., approximating R with the length of the longest semiaxis, seems to produce better results.

Again, we run the same cases for a value of the mesh size which is half of the previous one, and we notice that again the values σ_j^{opt1} do not change due to the change of the mesh size. The results are identical in terms of number of iterations to the case of the reference space discretization.

3. The fluid-structure interaction problem. In the second part of the work, we focus on the FSI problem. The analysis and optimization procedure we are going to show will allow us to develop effective RR algorithms for the solution of the FSI problem, when spherical-like interfaces separate fluid and structure. We are here interested in hemodynamics, in particular the FSI problem arising between blood and vessel wall in an abdominal aortic aneurysm, i.e., a pathological enlargement of the abdominal aorta which in many cases assumes an almost spherical-like shape [33, 39].

In the following sections, we will provide a convergence analysis for a simplified FSI problem and then report the convergence properties of some numerical experiments, for a spherical domain and for a real abdominal aortic aneurysm domain.

3.1. Problem setting. In view of the theoretical analysis, we consider a simplified problem arising from the interaction between the equations describing an incompressible, inviscid, and linear fluid occupying the sphere $\Omega_f = \{\mathbf{x} \in \mathbb{R}^3 : x^2 + y^2 + z^2 < R^2\}$ and the wave equation (used as a simplified model for the linear elastic structure problem) occupying the spherical shell $\Omega_s = \{\mathbf{x} \in \mathbb{R}^3 : R^2 < x^2 + y^2 + z^2 < (R+H)^2\}$. The two subproblems interact at the common interface $\Sigma = \{\mathbf{x} \in \mathbb{R}^3 : x^2 + y^2 + z^2 = R^2\}$. The external surface is denoted by Σ_{out} and \mathbf{n} is the outward unit normal.

The problem we are considering at discrete time $t^{n+1} = (n+1)\Delta t$ is the following:

$$\begin{aligned}
 (3.1a) \quad & \rho_f \delta_t \mathbf{u} + \nabla p = \mathbf{0} && \text{in } \Omega_f, \\
 (3.1b) \quad & \nabla \cdot \mathbf{u} = 0 && \text{in } \Omega_f, \\
 (3.1c) \quad & \mathbf{u} \cdot \mathbf{n} = \delta_t \boldsymbol{\eta} \cdot \mathbf{n} && \text{on } \Sigma, \\
 (3.1d) \quad & -p = \lambda \nabla \boldsymbol{\eta} \cdot \mathbf{n} && \text{on } \Sigma, \\
 (3.1e) \quad & \boldsymbol{\eta} \times \mathbf{n} = \mathbf{0} && \text{on } \Sigma, \\
 (3.1f) \quad & \rho_s \delta_{tt} \boldsymbol{\eta} - \lambda \Delta \boldsymbol{\eta} = \mathbf{0} && \text{in } \Omega_s, \\
 (3.1g) \quad & \gamma_{ST} \boldsymbol{\eta} + \lambda \nabla \boldsymbol{\eta} \cdot \mathbf{n} = P_{ext} \mathbf{n} && \text{on } \Sigma_{out},
 \end{aligned}$$

where \mathbf{u} and p stand for fluid velocity and pressure, $\boldsymbol{\eta}$ represents the structure displacement, ρ_f and ρ_s are the fluid and structure densities, λ is the coefficient related to the wave propagation that surrogates the elastic properties of the material, $\delta_t w = \frac{w - w^n}{\Delta t}$ and $\delta_{tt} w = \frac{\delta_t w - \delta_t w^n}{\Delta t}$, with Δt the time discretization step, and the current temporal index $n+1$ is understood. Equations (3.1a)–(3.1b) represent the fluid problem and (3.1f)–(3.1g) the structure problem equipped with a Robin condition at the external surface to account for the effect of an elastic surrounding tissue with elasticity modulus γ_{ST} . P_{ext} is an external pressure. Conditions (3.1c) and (3.1d) represent the coupling conditions at the fluid-structure interface. Notice that owing to the inviscid nature of the fluid, the coupling at the interface occurs only in the normal direction. For this reason, we have to complete the boundary conditions for the structure problem along the tangential direction, for example, by means of (3.1e).

Proceeding as above, we introduce two linear combinations of (3.1c) and (3.1d) by means of the interface operators S_f and S_s , obtaining the following generalized Robin interface conditions:

$$\begin{aligned} S_f u_r - p &= S_f \delta_t \eta_r + \lambda \partial_r \eta_r, \\ S_s \delta_t \eta_r + \lambda \partial_r \eta_r &= S_s u_r - p, \end{aligned}$$

where $u_r = \mathbf{u} \cdot \mathbf{n}$, $\eta_r = \boldsymbol{\eta} \cdot \mathbf{n}$. Rearranging the previous conditions, we can write them equivalently as follows:

$$(3.2a) \quad S_f \Delta t \delta_t u_r - p = \frac{S_f}{\Delta t} \eta_r + \lambda \partial_r \eta_r + F_1(u_r^n, \eta_r^n),$$

$$(3.2b) \quad \frac{S_s}{\Delta t} \eta_r + \lambda \partial_r \eta_r = S_s \Delta t \delta_t u_r - p + F_2(u_r^n, \eta_r^n),$$

where F_1 , F_2 contain terms at the previous time step n .

The FSI problem described by (3.1a)–(3.1g) can be equivalently rewritten by considering (3.2a) and (3.2b) as interface conditions. Thus, the generalized Schwarz algorithm corresponding to the problem given by (3.1a)–(3.1b)–(3.1e)–(3.1f)–(3.1g)–(3.2a)–(3.2b) reads as follows: Set $\eta_r^{(0)} = \eta_r^n$. Then, at each iteration $k > 0$, until convergence

1. solve the fluid problem,

$$(3.3a) \quad \rho_f \delta_t \mathbf{u}^{(k)} + \nabla p^{(k)} = \mathbf{0} \quad \text{in } \Omega_f,$$

$$(3.3b) \quad \nabla \cdot \mathbf{u}^{(k)} = 0 \quad \text{in } \Omega_f,$$

$$(3.3c) \quad S_f \Delta t \delta_t u_r^{(k)} - p^{(k)} = \frac{S_f}{\Delta t} \eta_r^{(k-1)} + \lambda \partial_r \eta_r^{(k-1)} + F_1(u_r^n, \eta_r^n) \quad \text{on } \Sigma;$$

2. then, solve the structure problem,

$$(3.4a) \quad \rho_s \delta_{tt} \boldsymbol{\eta}^{(k)} - \lambda \Delta \boldsymbol{\eta}^{(k)} = \mathbf{0} \quad \text{in } \Omega_s,$$

$$(3.4b) \quad \gamma_{ST} \boldsymbol{\eta}^{(k)} + \lambda \nabla \boldsymbol{\eta}^{(k)} \cdot \mathbf{n} = P_{ext} \mathbf{n} \quad \text{on } \Sigma_{out},$$

$$(3.4c) \quad \frac{S_s}{\Delta t} \eta_r^{(k)} + \lambda \partial_r \eta_r^{(k)} = S_s \Delta t \delta_t u_r^{(k)} - p^{(k)} + F_2(u_r^n, \eta_r^n) \quad \text{on } \Sigma,$$

$$(3.4d) \quad \boldsymbol{\eta}^{(k)} \times \mathbf{n} = \mathbf{0} \quad \text{on } \Sigma.$$

3.2. Convergence analysis. In view of the convergence analysis of the previous algorithm, we first note that as usual we can refer to the homogeneous case; thus we set to zero the quantities at previous time steps. Moreover, by applying the divergence operator to the first of (3.3), we face a Laplacian problem for the pressure solely. Finally, starting again from (3.3a), we exploit that at the interface

$$(\rho_f \delta_t \mathbf{u} + \nabla p) \cdot \mathbf{n} |_{\Sigma} = 0,$$

leading to

$$\partial_r p |_{\Sigma} = -\rho_f \delta_t u_r |_{\Sigma}.$$

From these observations, the generalized Schwarz algorithm (3.3)–(3.4) could be written as follows: Set $\eta_r^{(0)} = \eta_r^n$. Then, at each iteration $k > 0$, until convergence

1. solve the fluid problem,

$$(3.5a) \quad \Delta p^{(k)} = 0 \quad \text{in } \Omega_f,$$

$$(3.5b) \quad -S_f \frac{\Delta t}{\rho_f} \partial_r p^{(k)} - p^{(k)} = \frac{S_f}{\Delta t} \eta_r^{(k-1)} + \lambda \partial_r \eta_r^{(k-1)} \quad \text{on } \Sigma;$$

2. then, solve the structure problem,

$$(3.6a) \quad \frac{\rho_s}{\Delta t^2} \boldsymbol{\eta}^{(k)} - \lambda \Delta \boldsymbol{\eta}^{(k)} = \mathbf{0} \quad \text{in } \Omega_s,$$

$$(3.6b) \quad \gamma_{ST} \boldsymbol{\eta}^{(k)} + \lambda \nabla \boldsymbol{\eta}^{(k)} \cdot \mathbf{n} = P_{ext} \mathbf{n} \quad \text{on } \Sigma_{out},$$

$$(3.6c) \quad \frac{S_s}{\Delta t} \eta_r^{(k)} + \lambda \partial_r \eta_r^{(k)} = -S_s \frac{\Delta t}{\rho_f} \partial_r p^{(k)} - p^{(k)} \quad \text{on } \Sigma,$$

$$(3.6d) \quad \boldsymbol{\eta}^{(k)} \times \mathbf{n} = \mathbf{0} \quad \text{on } \Sigma.$$

We have the following result.

PROPOSITION 2. Set

$$(3.7) \quad A(m) = -\frac{\lambda \Delta t (2\beta R K'_{m+1/2}(\beta R) - K_{m+1/2}(\beta R) - \chi (2\beta R I'_{m+1/2}(\beta R) - I_{m+1/2}(\beta R)))}{2R (K_{m+1/2}(\beta R) - \chi I_{m+1/2}(\beta R))},$$

$$B(m) = -\frac{\rho_f R}{\Delta t m},$$

where we have set

$$(3.8) \quad \beta = \sqrt{\frac{\rho_s}{\lambda \Delta t^2}},$$

and

$$(3.9) \quad \chi(m) = \frac{2\gamma_{ST}(R+H)K_{m+1/2}(\beta(R+H)) + 2\lambda\beta(R+H)K'_{m+1/2}(\beta(R+H)) - \lambda K_{m+1/2}(\beta(R+H))}{2\gamma_{ST}(R+H)I_{m+1/2}(\beta(R+H)) + 2\lambda\beta(R+H)I'_{m+1/2}(\beta(R+H)) - \lambda I_{m+1/2}(\beta(R+H))}.$$

Then, the reduction factor of iterations (3.3)–(3.4) is given by

$$(3.10) \quad \rho(m) = \begin{cases} \left| \frac{\sigma_f(0) - A(0)}{\sigma_s(0) - A(0)} \right| & \text{if } m = 0, \\ \left| \frac{\sigma_f(m) - A(m)}{\sigma_s(m) - A(m)} \cdot \frac{\sigma_s(m) - B(m)}{\sigma_f(m) - B(m)} \right| & \text{if } m \neq 0, \end{cases}$$

where σ_f and σ_s are the symbols of \mathcal{S}_f and \mathcal{S}_s , respectively,

Proof. We start from the fluid problem. From (3.5) and applying the Fourier transform (2.6) with (2.5), we obtain the following ODEs in the variable r :

$$r^2 \frac{\partial^2 \hat{p}^{(k)}}{\partial r^2} + 2r \frac{\partial \hat{p}^{(k)}}{\partial r} - m(m+1)\hat{p}^{(k)} = 0.$$

The solution of the previous ODE is given by $\hat{p}^{(k)}(r, m, l) = X_{f,1}^{(k)}(m, l) r^m + X_{f,2}^{(k)}(m, l) r^{-m-1}$, for suitable functions $X_{f,1}^{(k)}$ and $X_{f,2}^{(k)}$. Since we assume that the pressure p is bounded for $r = 0$, we have

$$(3.11) \quad \hat{p}^{(k)}(r, m, l) = X_f^{(k)}(m, l) r^m.$$

Regarding the structure problem (3.4), by applying again the Fourier transform (2.6) and (2.5), we face an equation for η_r equal to (2.11) with $\frac{\rho_s}{\lambda \Delta t^2}$ instead of $\frac{\gamma}{\mu}$. Thus,

the solution is given by $\hat{\eta}_r^{(k)}(r, m, l) = X_{s,1}^{(k)}(m, l) \frac{I_{m+1/2}(\beta r)}{\sqrt{r}} + X_{s,2}^{(k)}(m, l) \frac{K_{m+1/2}(\beta r)}{\sqrt{r}}$ for suitable functions $X_{s,1}^{(k)}$ and $X_{s,2}^{(k)}$ and with β given by (3.8). Now, we impose condition (3.6b), leading to

$$\begin{aligned} & \gamma_{ST} \left(X_{s,1}^{(k)} \frac{I_{m+1/2}(\beta r)}{\sqrt{r}} + X_{s,2}^{(k)} \frac{K_{m+1/2}(\beta r)}{\sqrt{r}} \right) \\ & + \lambda \left(X_{s,1}^{(k)} \beta \frac{I'_{m+1/2}(\beta r)}{\sqrt{r}} - X_{s,1}^{(k)} \frac{I_{m+1/2}(\beta r)}{2\sqrt{r^3}} \right. \\ & \quad \left. + X_{s,2}^{(k)} \beta \frac{K'_{m+1/2}(\beta r)}{\sqrt{r}} - X_{s,2}^{(k)} \frac{K_{m+1/2}(\beta r)}{2\sqrt{r^3}} \right) \Big|_{r=R+H} = 0, \end{aligned}$$

and thus to $X_{s,1}^{(k)} = -\chi X_{s,2}^{(k)}$, where χ is given by (3.9). Therefore, the structure solution is

$$(3.12) \quad \hat{\eta}_r^{(k)}(r, m, l) = X_s^{(k)}(m, l) \frac{1}{\sqrt{r}} [K_{m+1/2}(\beta r) - \chi(m) I_{m+1/2}(\beta r)].$$

By inserting the solutions (3.11) and (3.12) into the interface conditions (3.5b)–(3.6c) and proceeding as in Proposition 1, the thesis follows. \square

3.3. Numerical results for the fluid-structure interaction problem.

3.3.1. Optimization procedure. In view of the numerical results, we need suitable values for the interface symbols S_f and S_s in the iterations (3.3)–(3.4). We proceed as done in section 2.3, i.e., we look for constant values along the straight line defined by (2.15), i.e., of the form

$$(3.13) \quad \begin{cases} \sigma_f = p, \\ \sigma_s = 2\bar{M} - p, \end{cases}$$

where p belongs to a suitable range $[p_-, p_+]$, and \bar{M} is given as in (2.14), with, however, A and B given by (3.7).

For the choice of the frequencies to be used in the optimization procedure, we consider all the frequencies $m \in [0, N - 1]$, with $N = \sqrt{n}$ and n the number of interface nodes (see strategy 1 in section 2.3).

3.3.2. Problem setting. We present in what follows the FSI problem we are going to consider to validate the theoretical findings of the previous section. In particular, we are interested in hemodynamics where the large *added mass effect* due to the similarity of the densities makes the convergence of partitioned algorithms very challenging [6, 31].

We consider the coupling between the Navier–Stokes equations for an incompressible fluid solved in the *arbitrary Lagrangian-Eulerian* formulation [11] and the linear infinitesimal elasticity. The main purpose here is to verify that the optimized interface parameters found for the simplified FSI problem analyzed in the previous section are effective also for the “complete” FSI problem. We have for each t

$$(3.14a) \quad \rho_f \partial_t^A \mathbf{u} + \rho_f ((\mathbf{u} - \boldsymbol{\omega}) \cdot \nabla) \mathbf{u} - \nabla \cdot \mathbf{T}_f(\mathbf{u}, p) = \mathbf{0} \quad \text{in } \Omega_f,$$

$$(3.14b) \quad \nabla \cdot \mathbf{u} = 0 \quad \text{in } \Omega_f,$$

$$(3.14c) \quad \rho_s \partial_{tt} \hat{\boldsymbol{\eta}} - \nabla \cdot \hat{\mathbf{T}}_s(\hat{\boldsymbol{\eta}}) = \mathbf{0} \quad \text{in } \hat{\Omega}_s,$$

$$(3.14d) \quad \mathbf{u} = \delta_t \boldsymbol{\eta} \quad \text{on } \Sigma,$$

$$(3.14e) \quad \mathbf{T}_f \mathbf{n} - \mathbf{T}_s \mathbf{n} = \mathbf{0} \quad \text{on } \Sigma,$$

where $\mathbf{T}_f(\mathbf{u}, p) = -p\mathbf{I} + \mu(\nabla\mathbf{u} + (\nabla\mathbf{u})^T)$ is the Cauchy stress tensor for the fluid, with μ the dynamic viscosity. Moreover, ∂_t^A represents the ALE derivative, i.e., the time derivative in the arbitrary Lagrangian-Eulerian framework, and $\boldsymbol{\omega}$ is the velocity of the fluid domain obtained by solving a harmonic extension of the interface velocity with homogeneous Dirichlet boundary conditions on $\Omega_f \setminus \Sigma$. Notice that, accordingly, Ω_f changes in time. Instead, the structure problem (3.14c) is solved in a Lagrangian framework and for this reason we have indicated with $\hat{\cdot}$ the corresponding quantities. Moreover, \mathbf{T}_s is the structure Cauchy stress tensor given by

$$\mathbf{T}_s(\boldsymbol{\eta}) = \lambda_1 (\nabla\boldsymbol{\eta} + (\nabla\boldsymbol{\eta})^T) + \lambda_2 (\nabla \cdot \boldsymbol{\eta}) \mathbf{I},$$

where λ_1 and λ_2 are the Lamé constants, that can be defined in terms of the Young modulus E and the Poisson ratio ν as follows:

$$\lambda_1 = \frac{E}{2(1+\nu)}, \quad \lambda_2 = \frac{\nu E}{(1+\nu)(1-2\nu)}.$$

We assume that the value of λ in the simplified structure problem (3.1f) is approximated by $\lambda = G\lambda_1$, where $G = \frac{\pi}{12}$ is the Timoshenko correction factor [17].

We use the following values for parameters: $\mu = 0.035 \text{ g}/(\text{cm s})$, $\rho_f = 1.0 \text{ g}/\text{cm}^3$, $\rho_s = 1.1 \text{ g}/\text{cm}^3$, $\nu = 0.49$, $E = 3 \cdot 10^6 \text{ dyne}/\text{cm}^2$, $\Delta t = 10^{-3} \text{ s}$. Accordingly, we have $\lambda = 8.3 \cdot 10^5 \text{ g}/(\text{cm s}^2)$.

We consider a backward Euler time discretization with a semi-implicit treatment of the convective term for the fluid and the BDF1 scheme for the structure. Moreover, we consider a semi-implicit treatment also for the geometric coupling, i.e., the fluid domain is found by extrapolation of previous time steps [4, 12, 30]. We use the pair of stable finite elements $P_{1,bubble} - P_1$ for the fluid subproblem and P_1 for the structure subproblem. The convergence of the RR algorithm has been monitored by evaluating at each iteration the following quantity [3]:

$$\int_{\Sigma} \sigma_f \left| \mathbf{u}^{(k)} - \delta_t \boldsymbol{\eta}^{(k)} \right| + \left| \mathbf{T}_f(\mathbf{u}^{(k)}, p^{(k)}) - \mathbf{T}_s(\boldsymbol{\eta}^{(k)}) \right| < \varepsilon,$$

where the value of the tolerance parameter ε has been set equal to 10^{-7} .

The numerical simulations have been performed with the finite elements library LifeV [1].

3.3.3. The case of spherical domain. We start considering an FSI test in a three-dimensional sphere cut at two opposite sides where the inlet and outlet planar sections Γ_{in} and Γ_{out} are located; see the corresponding fluid mesh in Figure 3.1. We have $R = 0.5 \text{ cm}$ and $H = 0.1 \text{ cm}$, and the meshes are such that the number of tetrahedra are about 33k for the fluid and 5k for the structure (total degrees of freedom about 55K). Moreover, we have $N = 38$. We have also considered a more refined mesh with about 41k tetrahedra for the fluid and 6k for the structure (total degrees of freedom about 76K, $N = 44$).

On the portion of Γ_{in} corresponding to the fluid domain, we prescribed the impulsive Neumann condition $\mathbf{T}_f(\mathbf{u}, p)\mathbf{n} = -P_{in}\mathbf{n}$, where

$$P_{in} = \begin{cases} 10 \text{ dyne}/\text{cm}^2 & \text{for } t < 0.008\text{s}, \\ 0 & \text{for } 0.008\text{s} \leq t \leq T, \end{cases}$$

where $T = 0.020 \text{ s}$. At the fluid outlet, we prescribed an absorbing boundary condition; see [30, 32]. For the structure, on both the inlet and outlet surfaces we prescribe

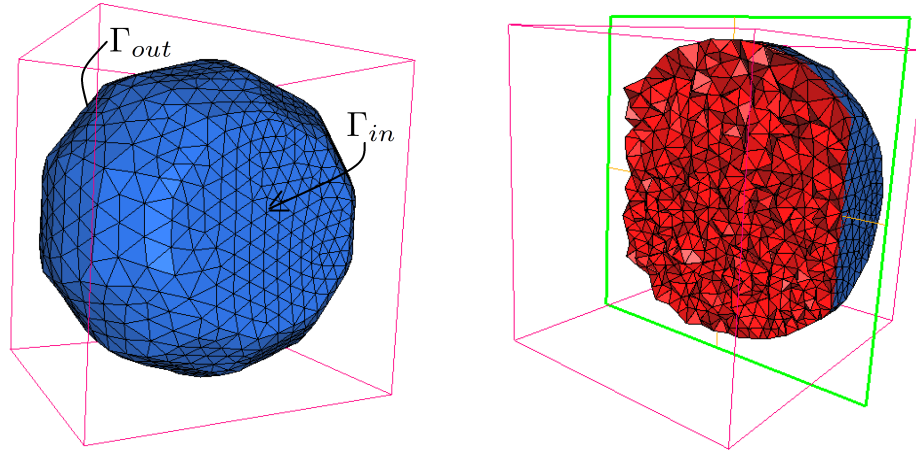
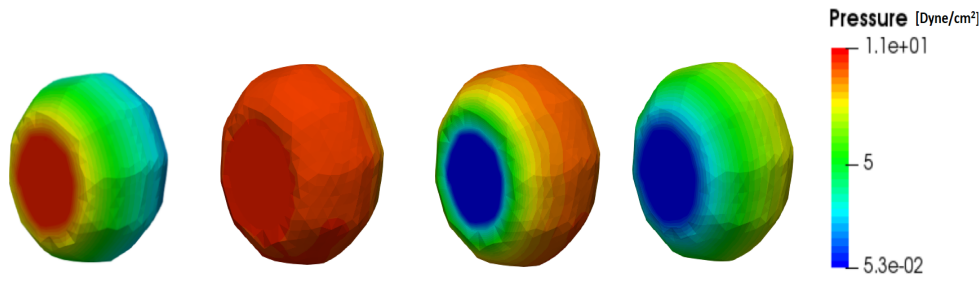


FIG. 3.1. Computational fluid mesh for the FSI test in the sphere.

FIG. 3.2. Pressure field at four different instants. From the left to the right: $t = 0.002\text{ s}$, $t = 0.006\text{ s}$, $t = 0.008\text{ s}$, $t = 0.010\text{ s}$. Γ_{in} on the left.

$\eta = \mathbf{0}$, i.e., we keep them fixed. Instead, at the external surface Γ_{ext} , we prescribe the Robin condition

$$\gamma_{ST}\hat{\mathbf{d}} + \hat{\mathbf{T}}_s(\hat{\mathbf{d}})\hat{\mathbf{n}} = \mathbf{0},$$

with $\gamma_{ST} = 1.5 \cdot 10^6 \text{ dyne/cm}^3$, to account for the effect of the surrounding tissue [29].

In Figure 3.2 we report the pressure field at four different instants. We observe, as expected, the traveling pressure wave which is absorbed at the outlet.

The optimization procedure on the straight line (3.13) leads to the estimation of the following optimized values: $\sigma_f = 1886.0$ and $\sigma_s = -17.3$. In Table 3.1 we report the convergence performance of the optimized RR scheme and of the DN scheme with an Aitken procedure. In particular, we consider variations of the Reynolds number (I and II rows), of Δt (I and III rows), and of the mesh (I and IV rows). The number of iterations is the average among the different time instants.

From these results we can observe a significant improvement of the convergence properties when optimized values of the interface parameters derived by our analysis are used in an RR scheme. In particular, this scheme works well in comparison to the DN scheme also for increased values of the Reynolds number and decreased values of Δt .

TABLE 3.1

Convergence performance for different values of P_{in} and Δt and different meshes. FSI test in the sphere.

	Method	σ_f/σ_s	# Iter
$P_{in}, \Delta t$ $N = 38$	Optimized RR DN+Aitken	1886.0/ - 17.3 $+\infty/0$	5.8 11.6
$100P_{in}, \Delta t$ $N = 38$	Optimized RR DN+Aitken	1886.0/ - 17.3 $+\infty/0$	7.8 14.1
$P_{in}, \Delta t/10$ $N = 38$	Optimized RR DN+Aitken	1002.2/ - 186.6 $+\infty/0$	15.2 28.6
$P_{in}, \Delta t$ $N = 44$	Optimized RR DN+Aitken	1887.4/ - 16.8 $+\infty/0$	5.9 11.9

TABLE 3.2

Values of the estimated optimized reduction factors ρ_{opt} and $\rho_{2,opt}$ for first and second order time approximations, respectively, as a function of Δt . FSI test in the sphere.

Δt	$\sigma_{f,opt}$	$\sigma_{s,opt}$	ρ_{opt}	$\sigma_{2,f,opt}$	$\sigma_{2,s,opt}$	$\rho_{2,opt}$
10^{-3}	1947.2	-77.6	0.033	1544.1	-96.6	0.052
10^{-4}	1049.4	-233.0	0.083	1425.1	-268.0	0.042
10^{-5}	986.7	-1365.9	0.006	1285.3	-2027.2	0.002
10^{-6}	955.8	-13512.2	0.0001	1274.9	-20270.6	0.00001

Notice also that the convergence properties of both RR and DN schemes deteriorate for decreasing values of Δt . This was expected for the DN scheme; indeed from (3.10) we have that $\lim_{\Delta t \rightarrow 0} \rho = 1$ when $\sigma_f = +\infty$ and $\sigma_s = 0$. Instead, for the RR scheme we could in principle choose σ_f and σ_s such that $\lim_{\Delta t \rightarrow 0} \rho < 1$. This is confirmed by the values reported in Table 3.2, first block, showing an a priori estimate of the optimized value ρ_{opt} of ρ along the straight line (3.13) and of the corresponding values of $\sigma_{f,opt}$ and $\sigma_{s,opt}$ (these being slightly different from those in Table 3.1 since the latter were estimated heuristically). These results show that the convergence properties of the RR scheme with optimized interface parameters deteriorate in accordance with the numerical results when $\Delta t \geq 10^{-4}$; however, they improve for smaller values of Δt .

In order to better understand the previous results, we performed the same convergence analysis of Proposition 2, where, however, second order time approximations are considered, in particular BDF2 for the fluid and kinematic condition, and Newmark (with parameters 1/2 and 1/4) for the structure. We found the following reduction factor (the computations are not reported for the sake of brevity):

$$\rho_2(m) = \begin{cases} \left| \frac{\sigma_f(0) - A_2(0)}{\sigma_s(0) - A_2(0)} \right| & \text{if } m = 0, \\ \left| \frac{\sigma_f(m) - A_2(m)}{\sigma_s(m) - A_2(m)} \cdot \frac{\sigma_s(m) - B_2(m)}{\sigma_f(m) - B_2(m)} \right| & \text{if } m \neq 0, \end{cases}$$

where $A_2(m) = 2/3A(m)$, $B_2(m) = 3/2B(m)$ (with A and B given by (3.7)), χ is given by (3.9), and β is replaced by $\beta_2 = 2\sqrt{\frac{\rho_s}{\lambda\Delta t^2}}$. In Table 3.2, second block, we report the a priori estimate of the optimized value $\rho_{2,opt}$ of ρ_2 along the straight line (3.13) and of the corresponding values of $\sigma_{2,f,opt}$ and $\sigma_{2,s,opt}$. From these results, we observe that for the second order time approximation, the values of the optimized reduction factor decrease with Δt .

Finally, we notice from last row of Table 3.1 that numerical experiments with different mesh size h highlighted that for both RR and DN methods the number of iterations is quite independent of h . This is in accordance with the theory of DN and RR preconditioners for the Schur complement equation [8, 37] and the numerical experiments reported in [3].

3.3.4. The case of an abdominal aortic aneurysm. In the second test, we aim at applying our optimization procedure for the RR scheme to a case of a real aortic aneurysm, namely one that develops at the abdominal level. These aneurysms could be in principle characterized by a balloon-like shape or could be fusiform, i.e., extended along the axial direction. In the first case, the almost spherical shape of the domain suggests the use of the analysis developed above to improve an FSI simulation.

To this aim, we consider the geometry of a real patient; see Figure 3.3. We use the same physical parameters and boundary conditions of the previous test case. The fluid and structure meshes are conforming at the interface and the number of tetrahedra is about 54k for the fluid and about 34k for the structure (total degrees of freedom about 100K). The values of the representative radius and thickness used in the optimization procedure are $R = 2.3\text{ cm}$ and $H = 0.1\text{ cm}$. Moreover, we have $N = 23$.

In Figure 3.4 we report the pressure field at four different instants. Again, as expected, the pressure wave travels along the domain and is absorbed at the outlet.

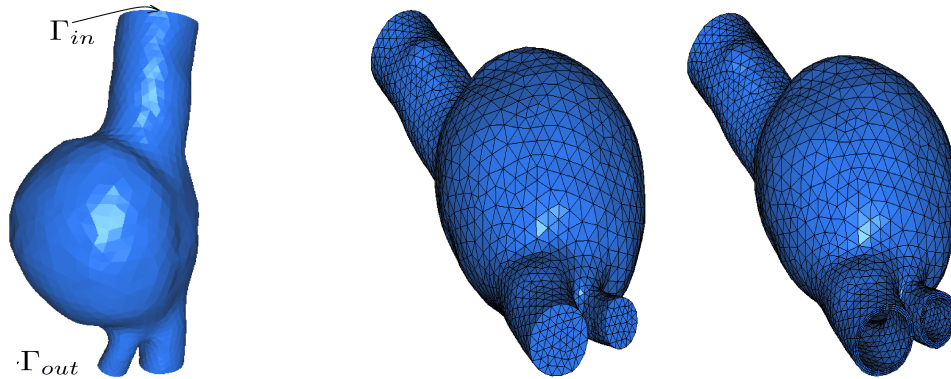


FIG. 3.3. Domain of the aortic aneurysm (left) and fluid and structure meshes (right).

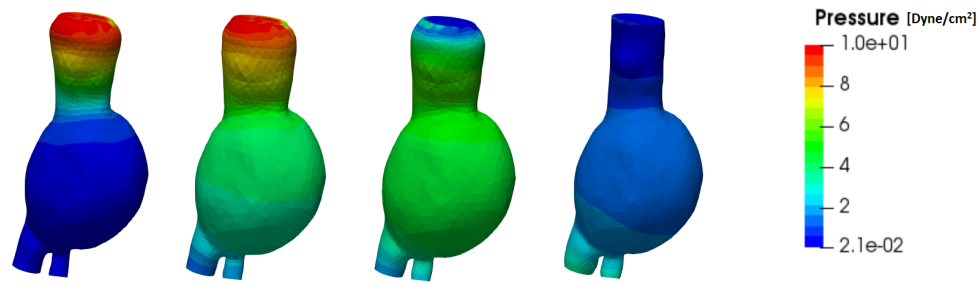


FIG. 3.4. Pressure field at four different instants. From the left to the right: $t = 0.002\text{ s}$, $t = 0.006\text{ s}$, $t = 0.008\text{ s}$, $t = 0.010\text{ s}$.

From the optimization procedure, we found that the optimized values are $\sigma_f = 1511.0$ and $\sigma_s = -143.4$. The number of iterations to reach convergence (average number among the different time instants) is in this case 12.0 against 15.6 needed by the DN-Aitken scheme. The improvement is more restrained in this case with respect to the previous test, probably because the geometry is not a perfect sphere as in the previous case. However, we have a speed-up of about 23%. This means that, since the number of iterations is quite independent of the mesh size, for more refined meshes needed for clinical applications, when the overall computational effort could be even of days, the speed-up of the RR scheme will be expected to be very significant.

REFERENCES

- [1] LIFEV, bitbucket.org/lifev-dev/lifev-release/wiki/Home, 2018.
- [2] S. ALI HASSAN, C. JAPHET, M. KERN, AND M. VOHRALÍK, *A posteriori stopping criteria for optimized Schwarz domain decomposition algorithms in mixed formulations*, Comput. Methods Appl. Math., 18 (2018), pp. 495–520.
- [3] S. BADIA, F. NOBILE, AND C. VERGARA, *Fluid-structure partitioned procedures based on Robin transmission conditions*, J. Comput. Phys., 227 (2008), pp. 7027–7051.
- [4] S. BADIA, A. QUAINI, AND A. QUATERONI, *Splitting methods based on algebraic factorization for fluid-structure interaction*, SIAM J. Sci. Comput., 30 (2008), pp. 1778–1805.
- [5] E. BLAYO, D. CHEREL, AND A. ROUSSEAU, *Towards optimized Schwarz methods for the navier–stokes equations*, J. Sci. Comput., 66 (2016), pp. 275–295.
- [6] P. CAUSIN, J. F. GERBEAU, AND F. NOBILE, *Added-mass effect in the design of partitioned algorithms for fluid-structure problems*, Comput. Methods Appl. Mech. Engrg., 194 (2005), pp. 4506–4527.
- [7] S. DEPARIS, *Numerical Analysis of Axisymmetric Flows and Methods for Fluid-Structure Interaction Arising in Blood Flow Simulation*, Ph.D. thesis, École Polytechnique Fédérale de Lausanne, 2004.
- [8] S. DEPARIS, M. DISCAGGIATI, G. FOURESTEY, AND A. QUATERONI, *Fluid-structure algorithms based on Steklov-Poincaré operators*, Comput. Methods Appl. Mech. Engrg., 195 (2006), pp. 5797–5812.
- [9] M. DISCAGGIATI AND L. GERARDO-GIORDA, *Optimized Schwarz methods for the stokes–darcy coupling*, IMA J. Numer. Anal., 38 (2018), pp. 1959–1983.
- [10] V. DOLEAN, M. J. GANDER, AND L. G. GIORDA, *Optimized Schwarz Methods for Maxwell's equations*, SIAM J. Sci. Comput., 31 (2009), pp. 2193–2213.
- [11] J. DONEA, *An arbitrary Lagrangian-Eulerian finite element method for transient dynamic fluid-structure interaction*, Comput. Methods Appl. Mech. Engrg., 33 (1982), pp. 689–723.
- [12] M. A. FERNÁNDEZ, J. F. GERBEAU, AND C. GRANDMONT, *A projection semi-implicit scheme for the coupling of an elastic structure with an incompressible fluid*, Internat. J. Numer. Methods Engrg., 69 (2007), pp. 794–821.
- [13] G. B. FOLLAND, *Introduction to Partial Differential Equations*, Princeton University Press, Princeton, NJ, 1995.
- [14] M. J. GANDER, *Optimized Schwarz methods*, SIAM J. Numer. Anal., 44 (2006), pp. 699–731.
- [15] M. J. GANDER AND Y. XU, *Optimized Schwarz methods for circular domain decompositions with overlap*, SIAM J. Numer. Anal., 52 (2014), pp. 1981–2004.
- [16] M. J. GANDER AND Y. XU, *Optimized Schwarz methods with nonoverlapping circular domain decomposition*, Math. Comp., 86 (2017), pp. 637–660.
- [17] L. GERARDO GIORDA, F. NOBILE, AND C. VERGARA, *Analysis and optimization of Robin-Robin partitioned procedures in fluid-structure interaction problems*, SIAM J. Numer. Anal., 48 (2010), pp. 2091–2116.
- [18] G. GIGANTE, M. POZZOLI, AND C. VERGARA, *Optimized Schwarz methods for the diffusion-reaction problem with cylindrical interfaces*, SIAM J. Numer. Anal., 51 (2013), pp. 3402–3420.
- [19] G. GIGANTE AND C. VERGARA, *Analysis and optimization of the generalized Schwarz method for elliptic problems with application to fluid-structure interaction*, Numer. Math., 131 (2015), pp. 369–404.
- [20] G. GIGANTE AND C. VERGARA, *Optimized Schwarz method for the fluid-structure interaction with cylindrical interfaces*, in Proceedings of the XXII International Conference on Domain Decomposition Methods, T. Dickopf, M. J. Gander, L. Halpern, R. Krause, and L. F. Pavarino, eds., Springer, New York, 2016, pp. 521–529.

- [21] G. GIGANTE AND C. VERGARA, *Optimized Schwarz methods for the coupling of cylindrical geometries along the axial direction*, Math. Model. Numer. Anal., 52 (2018), pp. 1597–1615.
- [22] C. JAPHET, *Optimized Krylov-Ventcell method. Application to convection-diffusion problems*, in Proceedings of the 9th International Conference on Domain Decomposition Methods, P. E. Bjorstad, M. S. Espedal, and D. E. Keyes, eds., 1998, pp. 382–389.
- [23] C. JAPHET AND F. NATAF, *The best interface conditions for domain decomposition methods: absorbing boundary conditions*, in Absorbing Boundaries and Layers, Domain Decomposition Methods, Nova Science, Huntington, NY, 2001, pp. 348–373.
- [24] N. LEBEDEV, *Special Functions and Their Applications*, Dover New York, 1972.
- [25] P. L. LIONS, *On the Schwarz alternating method III*, in Proceedings of the Third International Symposium on Domain Decomposition Methods for Partial Differential Equations, T. Chan, R. Glowinski, J. Periaux, and O. B. Widlund, eds., Proc. Appl. Math., SIAM, Philadelphia, 1990, pp. 202–223.
- [26] S. H. LUI, *A Lions non-overlapping domain decomposition method for domains with an arbitrary interface*, IMA J. Numer. Anal., 29 (2009), pp. 332–349.
- [27] F. MAGOULES, A. K. C. AHAMED, AND R. PUTANOWICZ, *Optimized Schwarz method without overlap for the gravitational potential equation on cluster of graphics processing unit*, Int. J. Comput. Math., 93 (2016), pp. 332–349.
- [28] F. MAGOULES, D. B. SZYLD, AND C. VENET, *Asynchronous optimized Schwarz methods with and without overlap*, Numer. Math., 137 (2017), pp. 199–227.
- [29] P. MOIREAU, N. XIAO, M. ASTORINO, C. A. FIGUEROA, D. CHAPELLE, C. A. TAYLOR, AND J.-F. GERBEAU, *External tissue support and fluid-structure simulation in blood flows*, Biomech. Model. Mechanobiol., 11 (2012), pp. 1–18, <https://doi.org/10.1007/s10237-011-0289-z>.
- [30] F. NOBILE, M. POZZOLI, AND C. VERGARA, *Time accurate partitioned algorithms for the solution of fluid-structure interaction problems in haemodynamics*, Comput. & Fluids, 86 (2013), pp. 470–482.
- [31] F. NOBILE, M. POZZOLI, AND C. VERGARA, *Inexact accurate partitioned algorithms for fluid-structure interaction problems with finite elasticity in haemodynamics*, J. Comput. Phys., 273 (2014), pp. 598–617.
- [32] F. NOBILE AND C. VERGARA, *An effective fluid-structure interaction formulation for vascular dynamics by generalized Robin conditions*, SIAM J. Sci. Comput., 30 (2008), pp. 731–763.
- [33] M. PICCINELLI, C. VERGARA, L. ANTIGA, L. FORZENIGO, P. BIONDETTI, AND M. DOMANIN, *Impact of hemodynamics on lumen boundary displacements in abdominal aortic aneurysms by means of dynamic computed tomography and computational fluid dynamics*, Biomech. Model. Mechanobiol., 12 (2013), pp. 1263–1276.
- [34] A. QADDOURI, L. LAAYOUNI, S. LOISEL, J. CÔTÉ, AND M. J. GANDER, *Optimized Schwarz methods with an overset grid for the shallow-water equations: preliminary results*, Appl. Numer. Math., 58 (2008), pp. 459–471.
- [35] A. QUARTERONI, L. DEDE', A. MANZONI, AND C. VERGARA, *Mathematical Modelling of the Human Cardiovascular System: Data, Numerical Approximation, Clinical Applications*, Cambridge University Press, Cambridge, UK, 2019.
- [36] A. QUARTERONI, R. SACCO, AND F. SALERI, *Numerical Mathematics*, Springer, Berlin, 2000.
- [37] A. QUARTERONI AND A. VALLI, *Domain Decomposition Methods for Partial Differential Equations*, Oxford Science Publications, New York, 1999.
- [38] B. STUPFEL, *Improved transmission conditions for a one-dimensional domain decomposition method applied to the solution of the Helmholtz equation*, J. Comput. Phys., 229 (2010), pp. 851–874.
- [39] C. A. TAYLOR, T. J. R. HUGHES, AND C. K. ZARINS, *Finite element analysis of pulsatile flow in the abdominal aorta under resting and exercise conditions*, American Society of Mechanical Engineers, Bioengineering Division, 33 (1996), pp. 81–82.
- [40] Y. YU, H. BAEK, AND G. E. KARNIADAKIS, *Generalized fictitious methods for fluid-structure interactions: Analysis and simulations*, J. Comput. Phys., 245 (2013), pp. 317–346.